A probability theory for filtered ghost imaging

Zhong-Yuan Liu(刘忠源), Shao-Ying Meng(孟少英), and Xi-Hao Chen(陈希浩)†

Key Laboratory of Optoelectronic Devices and Detection Technology, College of Physics, Liaoning University, Shenyang 110036, *China*

(Received 27 June 2022; revised manuscript received 28 September 2022; accepted manuscript online 7 October 2022)

Based on probability density functions, we present a theoretical model to explain filtered ghost imaging (FGI) we first proposed and experimentally demonstrated in 2017 [*Opt. Lett.* **42** 5290 (2017)]. An analytic expression for the joint intensity probability density functions of filtered random speckle fields is derived according to their probability distributions. Moreover, the normalized second-order intensity correlation functions are calculated for the three cases of low-pass, bandpass and high-pass filterings to study the resolution and visibility in the FGI system. Numerical simulations show that the resolution and visibility predicted by our model agree well with the experimental results, which also explains why FGI can achieve a super-resolution image and better visibility than traditional ghost imaging.

Keywords: filtered ghost imaging, probability density function, super-resolution

PACS: 42.30.Va, 42.30.Wb, 87.57.–s, 87.59.bd **DOI:** 10.1088/1674-1056/ac981e

1. Introduction

Ghost imaging (GI),[1] a novel imaging technique based on higher-order intensity correlation of optical fields, has been well studied theoretically and experimentally with both quantum and classical light sources in systems with and without focusing lenses.[1–8] Especially, GI for thermal light has shown great promise for development and has been realized by not only pseudo-thermal light[3,6] but also true thermal light[7,8] including sunlight.[9] During the rapid development of more than twenty years, the light sources have been expanded throughout the whole electromagnetic spectrum from visible light at the beginning to infrared[10] and x-rays,[11–13] while GI with particles such as atoms,[14] electrons[15] and even neutrons[16] has been realized due to its characteristic of lens-free imaging. In addition, many schemes have been proposed to overcome the drawbacks of low visibility and signal-to-noise ratio of the original setups, and to enhance resolution through methods including higher-order GI,[17] differential GI,[18] computational GI,[19] compressive GI,[20–22] correspondence imaging,[23] filtered GI (FGI),[24–27] GI via deep learning,[28–30] and their corresponding variations.

Theoretical investigations on GI began with both quantum and classical theories which came to the same main conclusion, and also led to some warm debate on whether the basic phenomenon is quantum or classical. Now, most researchers in the community believe that a classical explanation of GI is acceptable. Recently, the joint probability density function (PDF) of two optical intensities in GI has been employed to explain some newly observed experimental phenomena.[31–34] As an alternative theoretical method, this has some advantages in handling certain problems compared with previous methods. Cao *et al.* first derived the joint probability density function between the bucket and reference signals to explain the correspondence imaging experiment by probability theory and further discussed some new phenomena in thermal GI by the fractional-order moments of intensity.[31,32] Later, Yu *et al.* gave a theoretical discussion of the formation mechanism of correspondence imaging with thermal light via probability theory in statistical optics,[33] and Hu *et al.* investigated a Fourier-transform version by the joint probability density theory.[34]

Recently, a new approach for reconstructing super-resolution ghost images of targets in the FGI setup was experimentally demonstrated,[24–27] where the spatial resolution can exceed the Rayleigh diffraction limit by more than a factor of 10.[26] This newly proposed scheme of FGI offers an alternative potential method to improve the resolution, visibility and signal-to-noise ratio at the same time. However, the reason why these enhancements can be realized is unclear, and the theoretical explanation is left untouched, so this requires further consideration. Inspired by the papers[24–27,31–34] mentioned above, we present here a theoretical investigation based on probability theory, where an analytical expression for the joint probability density function in the FGI scheme is provided. On this basis, analytical expressions for the normalized second-order intensity correlation functions for the three cases of low-pass, bandpass and high-pass filterings of the optical intensities of thermal light are also obtained. By numerical simulation, it is shown that the predicted characteristics of the resolution and visibility are in good agreement with experimental results, which can be used to explain why FGI can exceed the diffraction limit and why it has better visibility.

The rest of this paper is organized as follows. In Section 2, according to the PDF of Rayleigh speckles, we introduce the PDF of the filtered intensity underlying the FGI schemes in Subsection 2.1, and then derive the joint PDFs for

†Corresponding author. E-mail: xi-haochen@163.com

© 2023 Chinese Physical Society and IOP Publishing Ltd

different filtering methods in Subsection 2.2. Based on this, in Subsection 3.1, we derive the normalized second-order intensity correlation functions to investigate the resolution in the FGI system, perform simulations in Subsection 3.2 to verify our theoretical results by comparison with the experimental results obtained before, and then in Subsection 3.3 give some theoretical derivations under certain limiting circumstances to explore the reason why the resolution and visibility are improved. In Subsection 4.1, we discuss the difference and relationship between a point object and a complex one in the FGI framework, and then in Subsection 4.2 discuss why FGI can overcome the diffraction limit to achieve a super-resolution image. In Section 5, we summarize the main results of the present work.

2. Joint probability density function of filtered intensities

2.1. The basic setup of FGI

A schematic diagram of FGI is shown in Fig. 1, which is essentially the same as that of the original FGI proposal.[24] As in most GI experiments, the pseudothermal source is generated by a laser beam incident on a rotating ground glass plate. The scattered light is divided into two beams by a beamsplitter. An object in the test beam is illuminated by the transmitted beam at a distance of z_1 from the source plane. After passing through the object the light signal is recorded by a spatially resolving detector such as a charge coupled device (CCD), which is followed by a spatial filter TF1 to filter the data pixel by pixel according to the preset thresholds.[24] Here, we consider CCD1 and TF1 as a detector system and they play the usual role of a GI bucket detector, from which the filtered signal is finally fed into the coincidence circuit after summed. Similarly, the reflected beam travels a distance z_2 from the source plane to the reference detector CCD2 to be directly recorded. After spatial intensity filtering by the filter TF2, the resulting reference signal is also fed into the coincidence circuit.

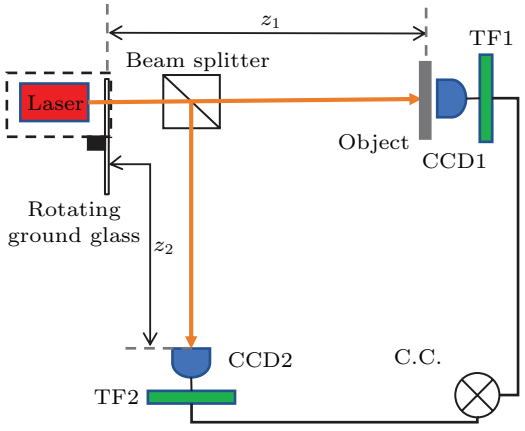


Fig. 1. Schematic diagram of FGI. CCD1 and CCD2, spatially resolving cameras; TF1 and TF2, spatial filters; z_1 and z_2, distances from the thermal source to the object plane and CCD2 plane, respectively.

It is well-known that the visibility and resolution in both GI and FGI systems are determined by the normalized second-order intensity correlation function, which has been widely studied after the historic Hanbury Brown and Twiss (HBT) experiment, and plays a similar role to the point spread function in conventional Fourier optics. Therefore, for the purpose of discussing why FGI can image an object with super-resolution and why its visibility can also be enhanced, we need to focus on the filtered HBT-like setup. The distances z_1 and z_2 between the source plane and the two detectors are equal. The instantaneous intensities I_i $(i=1,2)$ are the intensity distributions, $\bar{I}_i$ $(i=1,2)$ are their corresponding ensemble averages, and I_i' $(i=1,2)$ are the filtered intensity distributions in their respective detector planes. Here, indeed all the intensities are functions of spacetime, i.e., $I_i(r_i,t_i)$ and $I_i'(r_i,t_i)$ $(i=1,2)$. However, the variables r_i and t_i $(i=1,2)$ are ignored in most of the following derivations for brevity. TF1 and TF2 are also set identically for illustrating basic principles of FGI.

To provide a theoretical explanation of the previous experimental results,[24–26] we concentrate on three common types of filterings, i.e., bandpass, low-pass and high-pass filterings. Mathematically, the three cases are expressed as follows.

Case 1 Bandpass.

The filtered intensity is

$$I_i' = I_i \mathrm{rect}\left(\frac{2I_i-\beta_2-\beta_1}{2(\beta_2-\beta_1)}\right), \tag{1a}$$

where rect is the rectangle function and β_k $(k=1,2)$ are the upper and lower thresholds, respectively. It is obvious that $\beta_1<\beta_2$ is needed. Equation (1a) shows that, when $\beta_1 \le I \le \beta_2$, the intensity of I_i at a certain spacetime point keeps its value and this value is given to be I_i', i.e., $I_i'=I$, otherwise $I_i'=0$. Therefore, Eq. (1a) defines the bandpass filtering mathematically by virtue of the rectangle function.

Case 2 Low-pass.

Accordingly, when $\beta_1=0$ in Eq. (1a), the expression for the low-pass filtered intensity becomes

$$I_i' = I_i \mathrm{rect}\left(\frac{2I_i-\beta_2}{2\beta_2}\right). \tag{1b}$$

Case 3 High-pass.

Intuitively, from Eq. (1a) the expression for high-pass filtering should be obtained under the condition of $\beta_2\to\infty$. However, rect$(*)$ is not convergent at this time. Thus, the Heaviside step function of H$(*)$ is instead used to express the high-pass filtered intensity as

$$I_i' = I_i \mathrm{H}(I_i-\beta_1), \tag{1c}$$

where β_1 is the threshold. Clearly, $I_i'=I_i$ if $I_i\ge\beta_1$, otherwise $I_i'=0$, which represents the specific operation of high-pass filtering.

2.2. Expressions for the Joint PDF in FGI

The statistical behavior of a thermal field is usually referred to as Rayleigh statistics with a negative-exponential intensity PDF, which can be written explicitly as

$$p(I_i) = \frac{1}{\overline{I}_i} \exp\left(-\frac{I_i}{\overline{I}_i}\right). \tag{2}$$

For FGI, the role of the filtering is to keep the optical intensities unchanged within the range limited by the thresholds, but those beyond the range are set to be zero, which makes the possibility of zero intensities increase. For the sake of keeping the filtered PDF of I' normalized, the added possibility of zero intensities due to filtering should also be considered. Thus, according to Eq. (1), the filtered PDFs (see Appendix for details) in the above three bandwidth cases read

$$\begin{aligned} p_{\mathrm{b}}(I_i') &= p(I_i') \operatorname{rect}\left(\frac{2I_i' - \beta_2 - \beta_1}{2(\beta_2 - \beta_1)}\right) \\ &\quad + \delta(I_i')\left(\int_{\beta_2}^{\infty} \mathrm{d}I_i p(I_i) + \int_0^{\beta_1} \mathrm{d}I_i p(I_i)\right), \end{aligned} \tag{3a}$$

$$p_{\mathrm{l}}(I_i') = p(I_i') \operatorname{rect}\left(\frac{2I_i' - \beta_2}{2\beta_2}\right) + \delta(I_i') \int_{\beta_2}^{\infty} \mathrm{d}I_i p(I_i), \tag{3b}$$

$$p_{\mathrm{h}}(I_i') = p(I_i') H(I_i' - \beta_1) + \delta(I_i') \int_0^{\beta_1} \mathrm{d}I_i p(I_i), \tag{3c}$$

where p_j $(j = \mathrm{b}, \mathrm{l}, \mathrm{h})$ are the PDFs of cases 1–3, respectively. The Dirac functions in Eq. (3) are used so that the PDFs at $I' = 0$ become infinite but the corresponding probabilities, i.e., the integrals of PDFs in the neighbourhood of $I' = 0$, are finite. Here, it is required that $p_j(I')$ satisfies the normalization condition, i.e., $\int_0^{\infty} \mathrm{d}I_i' p_j(I_i') = 1$.

So far we have built the framework for the PDF of the filtered intensities. Next, the joint PDF is necessary to obtain the second-order correlation function in FGI. For thermal light, the joint PDF has been well studied,[34,35] and has the following expression for the intensities of I_1, I_2 at two space-time points,

$$\begin{aligned} p(I_1, I_2) &= \frac{1}{\overline{I}_1 \overline{I}_2 (1-\mu^2)} \exp\left\{-\frac{\overline{I}_1 I_2 + \overline{I}_2 I_1}{\overline{I}_1 \overline{I}_2 (1-\mu^2)}\right\} \\ &\quad \times J_0\left[\frac{2\mu\sqrt{I_1 I_2}}{\sqrt{\overline{I}_1 \overline{I}_2}(1-\mu^2)}\right], \end{aligned} \tag{4}$$

where $J_0(*)$ is the zeroth-order modified Bessel function of the first kind, $\overline{I}_1$ and $\overline{I}_2$ are the average intensities at two positions; μ is the modulus of the normalized first-order correlation function of the optical fields E_1 and E_2 at two points and is expressed as $\mu = |g_{12}^{(1)}| = \left|\frac{\langle E_1 E_2^* \rangle}{\sqrt{\langle |E_1|^2 \rangle \langle |E_2|^2 \rangle}}\right|$. As we know, the joint PDF is the key for the study of the second-order correlation of thermal light,[31,32,34] so it is also the key element for our filtered light fields. Basically, the joint PDF of the filtered intensities has the same form as Eq. (4) when $I_1' = I_1$ and $I_2' = I_2$ are satisfied within the threshold conditions. This means that $p_j(I_1', I_2') = p(I_1, I_2)$. Therefore, the joint PDFs (see Appendix for details) of $p_j(I_1', I_2')$ can be written as

$$\begin{aligned} &p_{\mathrm{b}}(I_1', I_2') \\ &= p(I_1', I_2') \operatorname{rect}\left(\frac{2I_1' - \beta_2 - \beta_1}{2(\beta_2 - \beta_1)}\right) \operatorname{rect}\left(\frac{2I_2' - \beta_2 - \beta_1}{2(\beta_2 - \beta_1)}\right) \\ &\quad + \delta(I_1') \int_0^{\infty} \mathrm{d}I_1' p(I_1', I_2') \left[1 - \operatorname{rect}\left(\frac{2I_1' - \beta_2 - \beta_1}{2(\beta_2 - \beta_1)}\right)\right] \\ &\quad + \delta(I_2') \int_0^{\infty} \mathrm{d}I_2' p(I_1', I_2') \left[1 - \operatorname{rect}\left(\frac{2I_2' - \beta_2 - \beta_1}{2(\beta_2 - \beta_1)}\right)\right] \\ &\quad + \delta(I_1')\delta(I_1') \int_0^{\infty}\int_0^{\infty} \mathrm{d}I_1' \mathrm{d}I_2' p(I_1', I_2') \\ &\quad \times \left[1 - \operatorname{rect}\left(\frac{2I_1' - \beta_2 - \beta_1}{2(\beta_2 - \beta_1)}\right)\right] \\ &\quad \times \left[1 - \operatorname{rect}\left(\frac{2I_2' - \beta_2 - \beta_1}{2(\beta_2 - \beta_1)}\right)\right], \end{aligned} \tag{5}$$

$$\begin{aligned} &p_{\mathrm{l}}(I_1', I_2') \\ &= p(I_1', I_2') \operatorname{rect}\left(\frac{2I_1' - \beta_2}{2\beta_2}\right) \operatorname{rect}\left(\frac{2I_2' - \beta_2}{2\beta_2}\right) \\ &\quad + \delta(I_1') \int_0^{\infty} \mathrm{d}I_1' p(I_1', I_2') \left[1 - \operatorname{rect}\left(\frac{2I_1' - \beta_2}{2\beta_2}\right)\right] \\ &\quad + \delta(I_2') \int_0^{\infty} \mathrm{d}I_2' p(I_1', I_2') \left[1 - \operatorname{rect}\left(\frac{2I_2' - \beta_2}{2\beta_2}\right)\right] \\ &\quad + \delta(I_1')\delta(I_1') \int_0^{\infty}\int_0^{\infty} \mathrm{d}I_1' \mathrm{d}I_2' p(I_1', I_2') \\ &\quad \times \left[1 - \operatorname{rect}\left(\frac{2I_1' - \beta_2}{2\beta_2}\right)\right] \left[1 - \operatorname{rect}\left(\frac{2I_2' - \beta_2}{2\beta_2}\right)\right], \end{aligned} \tag{6}$$

$$\begin{aligned} &p_{\mathrm{h}}(I_1', I_2') \\ &= p(I_1', I_2') H(I_1' - \beta_1) H(I_2' - \beta_1) \\ &\quad + \delta(I_1') \int_0^{\infty} \mathrm{d}I_1' p(I_1', I_2') \left[1 - H(I_1' - \beta_1)\right] \\ &\quad + \delta(I_2') \int_0^{\infty} \mathrm{d}I_2' p(I_1', I_2') \left[1 - H(I_2' - \beta_1)\right] \\ &\quad + \delta(I_1')\delta(I_1') \int_0^{\infty}\int_0^{\infty} \mathrm{d}I_1' \mathrm{d}I_2' p(I_1', I_2') \\ &\quad \times \left[1 - H(I_1' - \beta_1)\right] \left[1 - H(I_2' - \beta_1)\right]. \end{aligned} \tag{7}$$

3. Analytical expressions for the filtered HBT functions

In the framework of a GI (FGI) system, both the resolution and visibility are evaluated according to the normalized second-order correlation function $g_{12}^{(2)}(\boldsymbol{r}_1, \boldsymbol{r}_2)$, which also corresponds to an HBT-like measurement. In this section we will first derive analytical expressions for the filtered HBT measurements based on the joint PDF theory, then we will perform numerical HBT simulations for the three filter bands. In addition, we will give some theoretical derivations under various approximations. Finally, we will give a detailed analysis of the enhancement of resolution and visibility based on the simulation results.

3.1. The second-order correlation via the joint PDF

For the filtered HBT case, we have the following expression for the second-order correlation:

$$g_{12}^{(2)}(\boldsymbol{r}_1,\boldsymbol{r}_2)=\frac{\int_{\beta_1}^{\beta_2}\int_{\beta_1}^{\beta_2}\mathrm{d}I_1{}'\mathrm{d}I_2{}'\,I_1{}'I_2{}'p\,(I_1{}',I_2{}')}{\int_{\beta_1}^{\beta_2}\mathrm{d}I_1{}'\,I_1{}'p\,(I_1{}')\int_{\beta_1}^{\beta_2}\mathrm{d}I_2{}'\,I_2{}'p\,(I_2{}')}. \tag{8}$$

Based on the PDFs and joint PDFs obtained above, the second-order correlations for the three cases of bandpass (B), low-pass (L) and high-pass(H) can be expressed as follows:

$$\begin{aligned}\mathrm{B}:\ g_{12}^{(2)}&=\frac{\int_0^{\infty}\int_0^{\infty}\mathrm{d}I_1{}'\mathrm{d}I_2{}'\,I_1{}'I_2{}'p_{\mathrm{b}}\,(I_1{}',I_2{}')}{\int_0^{\infty}\mathrm{d}I_1{}'\,I_1{}'p_{\mathrm{b}}\,(I_1{}')\int_0^{\infty}\mathrm{d}I_2{}'\,I_2{}'p_{\mathrm{b}}\,(I_2{}')}\\&=\frac{\int_{\beta_1}^{\beta_2}\int_{\beta_1}^{\beta_2}\mathrm{d}I_1{}'\mathrm{d}I_2{}'\,I_1{}'I_2{}'p\,(I_1{}',I_2{}')}{\int_{\beta_1}^{\beta_2}\mathrm{d}I_1{}'\,I_1{}'p\,(I_1{}')\int_{\beta_1}^{\beta_2}\mathrm{d}I_2{}'\,I_2{}'p\,(I_2{}')}\\&=\int_{\beta_1}^{\beta_2}\int_{\beta_1}^{\beta_2}\mathrm{d}I_1{}'\mathrm{d}I_2{}'\,I_1{}'I_2{}'p\,(I_1{}',I_2{}')\\&\quad\times\left(\mathrm{e}^{-\frac{\beta_1}{\overline{I}_1}}(\overline{I}_1+\beta_1)-\mathrm{e}^{-\frac{\beta_2}{\overline{I}_1}}(\overline{I}_1+\beta_2)\right)^{-1}\\&\quad\times\left(\mathrm{e}^{-\frac{\beta_1}{\overline{I}_2}}(\overline{I}_2+\beta_1)-\mathrm{e}^{-\frac{\beta_2}{\overline{I}_2}}(\overline{I}_2+\beta_2)\right)^{-1},\end{aligned} \tag{9}$$

$$\mathrm{L}:\ g_{12}^{(2)}=\frac{\int_0^{\beta_2}\int_0^{\beta_2}\mathrm{d}I_1\,\mathrm{d}I_2\,I_1I_2p\,(I_1,I_2)}{\left(\overline{I}_1-\mathrm{e}^{-\frac{\beta_2}{\overline{I}_1}}(\overline{I}_1+\beta_2)\right)\left(\overline{I}_2-\mathrm{e}^{-\frac{\beta_2}{\overline{I}_2}}(\overline{I}_2+\beta_2)\right)}, \tag{10}$$

$$\mathrm{H}:\ g_{12}^{(2)}=\frac{\int_{\beta_1}^{\infty}\int_{\beta_1}^{\infty}\mathrm{d}I_1{}'\mathrm{d}I_2{}'I_1{}'I_2{}'p\,(I_1{}',I_2{}')}{\left(\mathrm{e}^{-\frac{\beta_1}{\overline{I}_1}}(\overline{I}_1+\beta_1)\right)\left(\mathrm{e}^{-\frac{\beta_1}{\overline{I}_2}}(\overline{I}_2+\beta_1)\right)}. \tag{11}$$

Though these expressions seem rather complex, it is not a problem when we perform numerical simulations. It should be noted that $\mu\neq 1$ because there is a singularity for the joint PDF and $g^{(2)}$ when $\mu=1$. However, this can be considered as a special case. When $\mu=1$, $g_{12}^{(2)}$ will become the autocorrelation function of the intensity, namely $g_{11}^{(2)}=\langle I_1'^2\rangle/\langle I_1'\rangle^2$, because the Cauchy–Schwarz inequality only takes the equal sign when E_1 is equal to E_2. The equations then become

$$\begin{aligned}\mathrm{B}:\ g_{11}^{(2)}&=\frac{\int_{\beta_1}^{\beta_2}\mathrm{d}I_1\,\frac{I_1^2}{\overline{I}_1}\mathrm{e}^{-\frac{I_1}{\overline{I}_1}}}{\left(\int_{\beta_1}^{\beta_2}\mathrm{d}I_1\frac{I_1}{\overline{I}_1}\mathrm{e}^{-\frac{I_1}{\overline{I}_1}}\right)^2}\\&=\frac{(2\overline{I}_1^2+2\overline{I}_1\beta_1+\beta_1^2)\,\mathrm{e}^{-\frac{\beta_1}{\overline{I}_1}}-(2\overline{I}_1^2+2\overline{I}_1\beta_2+\beta_2^2)\,\mathrm{e}^{-\frac{\beta_2}{\overline{I}_1}}}{\left[(\overline{I}_1+\beta_1)\,\mathrm{e}^{-\frac{\beta_1}{\overline{I}_1}}-(\overline{I}_1+\beta_2)\,\mathrm{e}^{-\frac{\beta_2}{\overline{I}_1}}\right]^2},\end{aligned}$$

$$\mathrm{L}:\ g_{11}^{(2)}=\frac{2\overline{I}_1^2-\left(2\overline{I}_1^2+2\overline{I}_1\beta_2+\beta_2^2\right)\mathrm{e}^{-\frac{\beta_2}{\overline{I}_1}}}{\left(\overline{I}_1-(\overline{I}_1+\beta_2)\,\mathrm{e}^{-\frac{\beta_2}{\overline{I}_1}}\right)^2}, \tag{12}$$

$$\mathrm{H}:\ g_{11}^{(2)}=\frac{(2\overline{I}_1^2+2\overline{I}_1\beta_1+\beta_1^2)\,\mathrm{e}^{\frac{\beta_1}{\overline{I}_1}}}{(\overline{I}_1+\beta_1)^2}. \tag{13}$$

The equations from Eqs. (9)–(13) are our main results. They indicate what role the filtering plays on the correlation by setting of the thresholds for the different cases. A clear physical picture will be shown in the next subsection by means of numerical simulations.

3.2. Simulations

To quantitatively verify the above theory and compare with the experimental results, we take the case of low-pass filtering as an example to perform some numerical simulations. The other two cases are similar and can be construed straightforwardly. In the simulation, we employ the same parameters as those in the published paper[24] to facilitate comparison with the experiment, where the thermal source has a diameter of 3 mm with a wavelength of 632.8 nm and the distance from the source to the detection plane is 240 mm. At the same time the experimental data of 30000 frames in Ref. [24] are also used to evaluate the influence of the parameters. As an example, we take $\overline{I}_1=\overline{I}_2=5.1$ (gray value). According to Eqs. (10) and (12), $g_{12}^{(2)}$ is first plotted for the two different cases shown in Fig. 2. Figure 2(a) shows how $g_{12}^{(2)}$ changes with respect to the threshold value β_2 and to the modulus of the first-order correlation function μ. When β_2 is not so small, for a given β_2, $g_{12}^{(2)}$ increases gradually to about 2 with the increase of μ just like $g^{(2)}$ in the original thermal light experiment. When μ is far away from 1 (e.g., $\mu<0.5$), for a given μ, $g_{12}^{(2)}$ changes very little with β_2. However, when μ is close to 1 and β_2 is small enough, a sudden sharp increase of $g_{12}^{(2)}$ occurs. In particular, when β_2 tends to 0 and μ tends to 1, $g_{12}^{(2)}$ seems to approach infinity. In general, when β_2 is small, the relation between μ and $g_{12}^{(2)}$ shows an obvious deviation from the Gaussian moment theorem.

Figure 2(b) provides a plot of $g_{12}^{(2)}$ with respect to β_2 and the one-dimensional coordinate r of the reference detector (pixel coordinate). Basically, $g_{12}^{(2)}$ ($g^{(2)}$) and μ are functions of the coordinate r because they are both functions of the optical field at certain spacetime points. We have omitted the co-ordinate variables above for simplicity, but here we have to consider the spatial coordinate r to study the spatial distribution of $g_{12}^{(2)}$. The modulus $\mu(r)$ in Eqs. (10) and (12) (where we need to substitute the $p\,(I_1,I_2)$ into the integrals) is first obtained according to the complex Gaussian moment theorem $\mu(r)=\sqrt{g^{(2)}(r)-1}/\sqrt{g^{(2)}(r)-1}\big|_{\max}$ [36] by calculating $g^{(2)}(r)$ using the experimental data mentioned above. The values of $\mu(r)$ thus obtained are then substituted into Eqs. (10) and (12) to plot Fig. 2(b). It can be seen that the trend of negligible dependence on β_2 is the same as that in Fig. 2(a), and $g_{12}^{(2)}$ also approaches its maximum when $\beta_2\to 0$ and $\mu\to 1$. This means that the visibility would be much improved when β_2 and μ are properly selected. This agrees well with the experimental results and can also be seen clearly in Fig. 3(a). To show more clearly how $g_{12}^{(2)}$ changes with β_2, Fig. 3(a) is plotted by setting $\mu=1$ according to Eq. (12), which also can be

regarded as a special case in Figs. 2(a) and 2(b). Actually, the curve of $g_{12}^{(2)}$ in Fig. 3(a) shows the maxima of $g_{12}^{(2)}$ for different β_2. It should be remarked that $g_{12}^{(2)}$ goes down to its minimum of about 1.8, which is less than 2, at the point $\beta_2 \approx 2.7\overline{I_1}$ before it turns sharply. When $\beta \approx 1.4\overline{I_1}$, the $g_{12}^{(2)}$ approaches to 2 as no filtering. This reflects how the visibility of an image in FGI changes with β_2. To improve the visibility of FGI in the low-pass case, β_2 should be set at least lower than $1.4\overline{I_1}$.

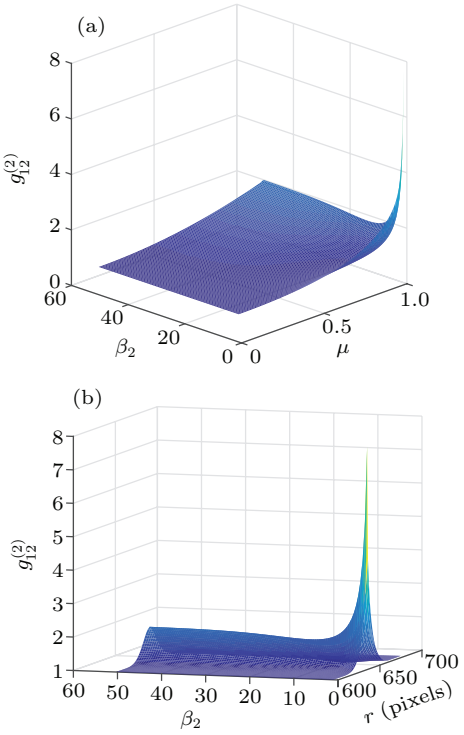


Fig. 2. Numerical simulations of $g_{12}^{(2)}$ for low-pass filtering: (a) $g_{12}^{(2)}$ versus β_2 and μ; (b) $g_{12}^{(2)}$ versus β_2 and r.

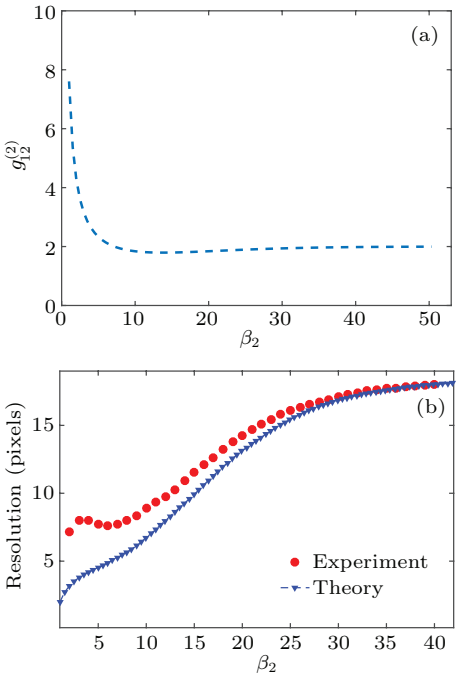


Fig. 3. (a) Behavior of $g_{12}^{(2)}$ versus β_2 at $\mu = 1$; (b) theoretical (blue dotted line) and experimental (red dots) data of the resolution versus β_2 at $\mu = 1$.

Another common important parameter of the resolution in FGI is determined by the full width at half maximum (FWHM) of $g_{12}^{(2)}$. This is numerically simulated by following the method of Fig. 2(b). The dependence of the FWHM of $g_{12}^{(2)}$, i.e., the resolution in FGI, with respect to the low-pass threshold of β_2 is shown in Fig. 3(b). The red dots are the experimental results[24] while the blue dotted line is the theoretical prediction. It can be seen that the theoretical and experimental varying trends of the resolution are generally in good agreement, apart from the deviations at the low thresholds. It is found that the resolution in both the cases increases with the decrease of β_2 and dramatically increases when β_2 becomes small enough.

3.3. Further theoretical derivation through some approximations

In the previous simulation we have seen that, as $g_{12}^{(2)}$ varies with respect to β_2 and μ, a significant change occurs in a certain region where β_2 is small and μ is close to 1. However, this seems not so explicit in the present theoretical formulation so some further adjustment is needed. Therefore, in this subsection, we will further extend our model by adding some appropriate approximations to investigate why our technique can achieve super-resolution images together with much higher visibility.

First, we consider the case of low-pass filtering. The Taylor series expansion of Eqs. (10) and (12) can be applied if β_2 is small enough. After higher order items are ignored and $\frac{\beta_2}{\overline{I_1}}\frac{1}{1-\mu^2} \ll 1$ is satisfied, the equations become

$$\begin{aligned} \mathrm{L}:\ g_{12}^{(2)} &\approx \frac{1}{1-\mu^2}\left(1+\frac{2\beta_2}{3\overline{I_1}}+\frac{2\beta_2}{3\overline{I_2}}\right. \\ &\quad \left.-\frac{2\beta_2}{3\overline{I_1}(1-\mu^2)}-\frac{2\beta_2}{3\overline{I_2}(1-\mu^2)}\right) \\ &\approx \frac{1}{1-\mu^2}, \end{aligned} \tag{14}$$

and when $\mu = 1$,

$$\mathrm{L}:\ g_{11}^{(2)} \approx \frac{4\overline{I_1}}{3\beta_2}+\frac{7}{9}. \tag{15}$$

It can be seen from Eqs. (14) and (15) that $g_{12}^{(2)}$ could be much larger than 2 if μ is close to 1 or β_2 is close to 0 when $\mu = 1$. Especially, in the latter case, $g_{11}^{(2)}$ is inversely proportional to β_2, which causes its maximum to become much larger with the decrease of β_2, but its values at other positions do not change so much. Therefore, the FWHM of the $g_{11}^{(2)}$ peak will shrink while the visibility will increase at the same time. This demonstrates the role that the filtering plays and why a super-resolution image can be achieved with a visibility as high as 100%. Importantly, $g_{11}^{(2)} > 2$ actually embodies a non-Rayleigh characteristic of the filtered field, which will be discussed in Subsection 4.2.

4. Discussion

4.1. Super-resolution imaging by FGI

What we have discussed above is based on the HBT-like system where no bucket detector is needed, which can be seen as a special case of imaging a point object. However, a bucket detector is necessary in an actual GI system, so the difference between imaging a point object and an actual object should be further clarified. For example, although some algorithms can resolve a point object with super-resolution,[37,38] they would not work when a complicated object is to be imaged or the image is not a simple superposition of many component points. For simplicity and generality, we take a binary transmission object as an example. In Fig. 1, if the transmission area of the object is S, the corresponding ghost image is given by

$$g_S^{(2)}(\boldsymbol{r}_2) = \frac{\left\langle \int_S \mathrm{d}^2\boldsymbol{r}_1 I_1'(\boldsymbol{r}_1) I_2'(\boldsymbol{r}_2)\right\rangle}{\left\langle \int_S \mathrm{d}^2\boldsymbol{r}_1 I_1'(\boldsymbol{r}_1)\right\rangle \left\langle I_2'(\boldsymbol{r}_2)\right\rangle}. \tag{16}$$

It is well-known that for a uniform incoherent source, its average intensity I_0 is uniform under the Fresnel approximation. Thus, the intensity in both beams can be expressed as

$$\langle I_1\rangle = \langle I_2\rangle = \int \mathrm{d}^2\boldsymbol{r}_1 I_0 \frac{1}{\lambda^2 z^2}. \tag{17}$$

After filtering, the equation still holds, namely,

$$\left\langle I_1'\right\rangle = \left\langle I_2'\right\rangle = \text{const.} \tag{18}$$

Hence, Eq. (16) becomes

$$g_S^{(2)}(\boldsymbol{r}_2) = \frac{1}{S}\int_S \mathrm{d}^2\boldsymbol{r}_1 g_{12}^{(2)}(\boldsymbol{r}_1,\boldsymbol{r}_2). \tag{19}$$

It is clear that the super-resolution image $g_S^{(2)}(\boldsymbol{r}_2)$ in FGI is simply a linear superposition of point images $g_{12}^{(2)}(\boldsymbol{r}_1,\boldsymbol{r}_2)$. The role that $g_{12}^{(2)}(\boldsymbol{r}_1,\boldsymbol{r}_2)$ plays here is somewhat like the point spread function in classical imaging and traditional GI.[39,40] This means that the resolution of an FGI system is completely determined by $g_{12}^{(2)}(\boldsymbol{r}_1,\boldsymbol{r}_2)$, just as discussed above. Consequently, FGI can surpass the diffraction limit set by the numerical aperture of the imaging system and achieve a super-resolution image of a target object if the FWHM of $g_{12}^{(2)}(\boldsymbol{r}_1,\boldsymbol{r}_2)$ can become narrower than that of $g_{12}^{(2)}(\boldsymbol{r}_1,\boldsymbol{r}_2)$ of the original thermal field.

4.2. Further explanation and discussion of super-resolution

In fact, our strategy to achieve super-resolution is to minimize the broadening of the second-order correlation function caused by the finite aperture of the light source compared with a completely incoherent source. For a completely incoherent source, μ should be similar in form to a δ function, and $g^{(2)} = 1 + |\mu|^2 \propto \delta$ would be satisfied. However, since the aperture of an actual imaging system can only be finite, μ does not have the form of δ. For a light source with a diameter of d, we have $\mu \propto \left|\delta(r) \otimes \mathscr{F}\left\{\mathrm{circ}\left(\frac{r}{d/2}\right)\right\}\right|$, where $\otimes$ represents convolution, $\mathrm{circ}(*)$ is the circle function and r is the distance between two arbitrary points in the detection plane. The finite aperture causes μ to lose its Dirac δ function form after convolution, and correspondingly it also broadens $g^{(2)}$, making it even less like a δ function. However, the higher order terms of μ show better resolution and less deviation from Dirac function.

The shape of $\mu(r)$ and the PDF of the light field together determine the FWHM of $g^{(2)}$. The strategy, FGI, does not affect the propagation of the light but detects the physical signals in a different way. More inherently, FGI changes the joint PDF, finally transforming the relation between $g^{(2)}$ and μ into different formulations. In general, more high-order items of μ appear in $g^{(2)}$, which will improve the resolution. Explicitly, for example, Eq. (14) can be rewritten as $g^{(2)} = 1 + \mu^2 + \mu^4 + \cdots$. Here, the Gaussian moment theorem is no longer satisfied. High order items of μ are mixed with the same weight, thus super-resolution images can be achieved. From the perspective of the speckles, filtering changes the original Rayleigh speckle field to the non-Rayleigh, which greatly changes the topological structure of speckles. This may also inspire us to change the intensity correlation of an optical field by a different method besides the intensity filtering to improve the performance of GI systems, especially with regard to the resolution and visibility.

5. Conclusion

In summary, we have provided a theoretical model based on the concept of the joint PDF to explain why FGI can achieve a super-resolution image with a higher visibility. Numerical simulations of low-pass filtering as an example have shown that the theoretical predictions are in good agreement with the experimental results. It is interesting that at $\mu = 1$ and as the low-pass threshold β_2 decreases, the minimum values of $g_{12}^{(2)}$ remain stable but its maximum gradually decreases from the theoretical value of 2 to about 1.8 and then suddenly rises sharply to a value that is much larger than 2 when β_2 approaches 0. This change not only contributes to the visibility improvement but also to the resolution enhancement, especially for the sharp improvement to one pixel[24] when β_2 is small enough. According to our analysis, the relationship between $g_{12}^{(2)}$ and μ changes under certain conditions (see Eq. (14)) because of filtering, which is the basic reason for the resolution and visibility improvement. Actually, intensity filtering changes the probability density function, which changes the correlation. Though not all types of methods to change the probability can guarantee that the correlation would become larger and narrower, our model suggests that

we could design various optical fields with different probabilities and customized intensity speckles which would be even better for achieving super-resolution imaging. Although a post-processing method is necessary in our current experimental setup, this is just due to the technical limitation to produce a light field of such PDFs or to directly detect bucket signal after filtered. In fact, it offers a potentially promising scheme for applications in all fields of imaging by using customized speckles, which could be generated, for example, by a spatial light modulator.

Appendix A

In this appendix we will take the low-pass case as an example to show how PDF and joint PDF in the filtered GI systems are deduced. Those for the high-pass and band-pass cases will be straightforward. As we know, filtering is based on the thermal field that its intensity meets a probability of a negative-exponential intensity PDF shown in Eq. (2). Therefore, for the low-pass filtering, the PDF is unchanged, i.e., $p_1(I_i') = p(I_i)$ when $0 < I_i' = I_i < \beta_2$, while $p_1(I_i') = 0$ because of filtering when $I_i' \geqslant \beta_2$. However, it should be noted that the probability of this fraction will contribute to the probability $p_1(0)$, which comes from the filtering. Considering the contribution of both the filterings, i.e., $p(I_i \to I_i' = 0)$ and $p(I_i = 0)$, the probability after filtering in the neighborhood of $I_i' = 0$ can be expressed as

$$p_1(0)\,\mathrm{d}I_i' = p(0)\,\mathrm{d}I_i' + \int_{\beta_2}^{\infty} p(I_i)\,\mathrm{d}I_i. \tag{A1}$$

Mathematically, $\mathrm{d}I_i'$ is an infinitesimal quantity, which leads the PDF at $I_i' = 0$ to be infinity. Thus, we can obtain the expression of PDF as

$$p_1(0) = p(0) + \delta(0)\int_{\beta_2}^{\infty} p(I_i)\,\mathrm{d}I_i. \tag{A2}$$

After considering the cases of $I_i' = 0$ (A2) and $0 < I_i' < \beta_2$ together, the filtered PDF is expressed as

$$p_1(I_i') = p\left(I_i'\right)\mathrm{rect}\left(\frac{2I_i' - \beta_2}{2\beta_2}\right) + \delta\left(I_i'\right)\int_{\beta_2}^{\infty}\mathrm{d}I_i p(I_i), \tag{A3}$$

where the rectangle function can be explicitly written as

$$\mathrm{rect}(x) = \begin{cases} 1, & |x| < \frac{1}{2}; \\ \frac{1}{2}, & |x| = \frac{1}{2}; \\ 0, & \text{otherwise.} \end{cases} \tag{A4}$$

Following the similar process, the PDFs for the bandpass and high-pass cases can be expressed as

$$p_{\mathrm{b}}\left(I_i'\right) = p\left(I_i'\right)\mathrm{rect}\left(\frac{2I_i' - \beta_2 - \beta_1}{2(\beta_2 - \beta_1)}\right) + \delta\left(I_i'\right)\left(\int_{\beta_2}^{\infty}\mathrm{d}I_i p(I_i) + \int_0^{\beta_1}\mathrm{d}I_i p(I_i)\right), \tag{A5}$$

$$p_{\mathrm{h}}\left(I_i'\right) = p\left(I_i'\right)\mathrm{H}\left(I_i' - \beta_1\right) + \delta\left(I_i'\right)\int_0^{\beta_1}\mathrm{d}I_i p(I_i). \tag{A6}$$

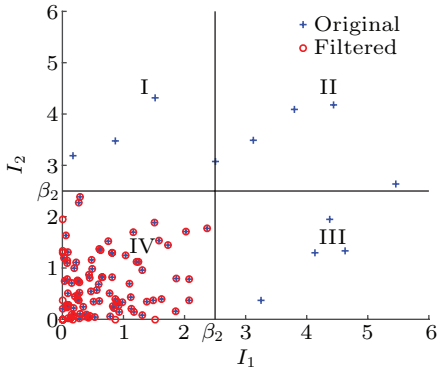


Fig. A1. Scatter plot for the intensity distributions before (blue plus signs) and after (red circles) filtering.

Similarly, the joint PDF can be deduced, though it is slightly more complicated. To illustrate it more comprehensibly, we draw a scatter plot shown in Fig. A1 according to the Eq. (4), where the sparsity of 100 random points that are denoted by blue pluses represents the joint PDF $p(I_1, I_2)$. It can be seen that all the points of pluses are distributed in the first quadrant and on the axes of coordinates because the intensities must be not negative. Then the filtered PDF $p_1(I_1', I_2')$ is represented by the sparsity of red circles when $\beta_2 = 2.5$. Otherwise, $\mu = 0.3$ and $\overline{I_1} = \overline{I_2} = 1$ have been set in the plot. It is obvious that by the low-pass threshold of β_2 we can divide the first quadrant into four areas as follows:

$$\begin{aligned} &\mathrm{I}: && I_1 < \beta_2, I_2 \geqslant \beta_2; \\ &\mathrm{II}: && I_1 \geqslant \beta_2, I_2 \geqslant \beta_2; \\ &\mathrm{III}: && I_1 \geqslant \beta_2, I_2 < \beta_2; \\ &\mathrm{IV}: && 0 < I_1 < \beta_2, 0 < I_2 < \beta_2. \end{aligned}$$

From Fig. A1, we can know that the blue pluses in area IV are transformed into red circles after filtering while in I, II and III, the pluses are removed and transferred onto the axes of I_1, I_2 and origin of coordinates, respectively. Therefore, the filtered joint probabilities can be expressed as

$$\begin{cases} p_1(I_1', I_2')\,\mathrm{d}I_1'\,\mathrm{d}I_2' = 0, & (I_1', I_2') \in \mathrm{I}\text{–}\mathrm{III}, \\ p_1(I_1', I_2')\,\mathrm{d}I_1'\,\mathrm{d}I_2' = p(I_1', I_2')\,\mathrm{d}I_1'\,\mathrm{d}I_2', & (I_1', I_2') \in \mathrm{IV}, \\ p_1(0, I_2')\,\mathrm{d}I_1'\,\mathrm{d}I_2' = p(0, I_2')\,\mathrm{d}I_1'\,\mathrm{d}I_2' + \mathrm{d}I_2'\int_{\beta_2}^{\infty}\mathrm{d}I_1' p(I_1', I_2'), & (I_1' = 0,\ I_2' \neq 0), \\ p_1(I_1', 0)\,\mathrm{d}I_1'\,\mathrm{d}I_2' = p(I_1', 0)\,\mathrm{d}I_1'\,\mathrm{d}I_2' + \mathrm{d}I_1'\int_{\beta_2}^{\infty}\mathrm{d}I_2' p(I_1', I_2'), & (I_1' \neq 0,\ I_2' = 0), \\ p_1(0,0)\,\mathrm{d}I_1'\,\mathrm{d}I_2' = p(0,0)\,\mathrm{d}I_1'\,\mathrm{d}I_2' + \int_{\beta_2}^{\infty}\int_{\beta_2}^{\infty}\mathrm{d}I_1'\,\mathrm{d}I_2' p(I_1',\ I_2'), & (I_1' = 0,\ I_2' = 0). \end{cases} \tag{A7}$$

and the corresponding joint PDFs can be written as

$$\begin{cases} p_1(I_1',I_2') = 0, & (I_1',I_2') \in \text{I–III}, \\ p_1(I_1',I_2') = p(I_1',I_2'), & (I_1',\ I_2') \in \text{IV}, \\ p_1(0,I_2') = p(0,I_2') + \delta(I_1') \int_{\beta_2}^{\infty} \mathrm{d}I_1' p(I_1',I_2'), & (I_1'=0,\ I_2' \neq 0), \\ p_1(I_1',0) = p(I_1',0) + \delta(I_2') \int_{\beta_2}^{\infty} \mathrm{d}I_2' p(I_1',I_2'), & (I_1' \neq 0,\ I_2'=0), \\ p_1(0,0) = p(0,0) + \delta(I_1')\,\delta(I_2') \int_{\beta_2}^{\infty}\int_{\beta_2}^{\infty} \mathrm{d}I_1'\mathrm{d}I_2' p(I_1',I_2'), & (I_1'=0,\ I_2'=0). \end{cases} \tag{A8}$$

Finally, a more compact expression of the joint PDF for the low-pass case is given by

$$\begin{aligned} p_1(I_1',I_2') = {} & p(I_1',I_2')\,\mathrm{rect}\left(\frac{2I_1'-\beta_2}{2\beta_2}\right)\mathrm{rect}\left(\frac{2I_2'-\beta_2}{2\beta_2}\right) + \delta(I_1')\int_0^{\infty}\mathrm{d}I_1' p(I_1',I_2')\left[1-\mathrm{rect}\left(\frac{2I_1'-\beta_2}{2\beta_2}\right)\right] \\ & + \delta(I_2')\int_0^{\infty}\mathrm{d}I_2' p(I_1',I_2')\left[1-\mathrm{rect}\left(\frac{2I_2'-\beta_2}{2\beta_2}\right)\right] + \delta(I_1')\,\delta(I_1')\int_0^{\infty}\int_0^{\infty}\mathrm{d}I_1'\mathrm{d}I_2' p(I_1',I_2') \\ & \times\left[1-\mathrm{rect}\left(\frac{2I_1'-\beta_2}{2\beta_2}\right)\right]\left[1-\mathrm{rect}\left(\frac{2I_2'-\beta_2}{2\beta_2}\right)\right]. \end{aligned} \tag{A9}$$

The similar procedures can be taken for the bandpass and high-pass cases. The joint PDFs can be written as

$$\begin{aligned} p_{\mathrm{b}}(I_1',I_2') = {} & p(I_1',I_2')\,\mathrm{rect}\left(\frac{2I_1'-\beta_2-\beta_1}{2(\beta_2-\beta_1)}\right)\mathrm{rect}\left(\frac{2I_2'-\beta_2-\beta_1}{2(\beta_2-\beta_1)}\right) + \delta(I_1')\int_0^{\infty}\mathrm{d}I_1' p(I_1',I_2')\left[1-\mathrm{rect}\left(\frac{2I_1'-\beta_2-\beta_1}{2(\beta_2-\beta_1)}\right)\right] \\ & + \delta(I_2')\int_0^{\infty}\mathrm{d}I_2' p(I_1',I_2')\left[1-\mathrm{rect}\left(\frac{2I_2'-\beta_2-\beta_1}{2(\beta_2-\beta_1)}\right)\right] + \delta(I_1')\,\delta(I_1')\int_0^{\infty}\int_0^{\infty}\mathrm{d}I_1'\mathrm{d}I_2' p(I_1',I_2') \\ & \times\left[1-\mathrm{rect}\left(\frac{2I_1'-\beta_2-\beta_1}{2(\beta_2-\beta_1)}\right)\right]\left[1-\mathrm{rect}\left(\frac{2I_2'-\beta_2-\beta_1}{2(\beta_2-\beta_1)}\right)\right], \end{aligned} \tag{A10}$$

$$\begin{aligned} p_{\mathrm{h}}(I_1',I_2') = {} & p(I_1',I_2')\,\mathrm{H}(I_1'-\beta_1)\,\mathrm{H}(I_2'-\beta_1) + \delta(I_1')\int_0^{\infty}\mathrm{d}I_1' p(I_1',I_2')\left[1-\mathrm{H}(I_1'-\beta_1)\right] \\ & + \delta(I_2')\int_0^{\infty}\mathrm{d}I_2' p(I_1',I_2')\left[1-\mathrm{H}(I_2'-\beta_1)\right] + \delta(I_1')\,\delta(I_1')\int_0^{\infty}\int_0^{\infty}\mathrm{d}I_1'\mathrm{d}I_2' p(I_1',I_2') \\ & \times\left[1-\mathrm{H}(I_1'-\beta_1)\right]\left[1-\mathrm{H}(I_2'-\beta_1)\right]. \end{aligned} \tag{A11}$$

Acknowledgements

We thank Professor L. A. Wu for helpful discussion.

Project supported by the National Key Research and Development Program of China (Grant No. 2018YFB0504302), and the Project of Innovation and Entrepreneurship Training Program for college students of Liaoning University (Grant No. S202110140003).

References

[1] Pittman T, Shih Y H, Strekalov D and Sergienko A 1995 *Phys. Rev. A* **52** R3429
[2] Cheng J and Han S 2004 *Phys. Rev. Lett.* **92** 093903
[3] Gatti A, Brambilla A E, Bache M and Lugiato L A 2004 *Phys. Rev. Lett.* **93** 093602
[4] Cai J Y and Zhu S Y 2005 *Phys. Rev. E* **71** 056607
[5] Cao D Z, Xiong J and Wang K G 2005 *Phys. Rev. A* **71** 013801
[6] Valencia A, Scarcelli G, D'Angelo M and Shih Y 2005 *Phys. Rev. Lett.* **94** 063601
[7] Zhang D, Zhai Y H, Wu L A and Chen X H 2005 *Opt. Lett.* **30** 2354
[8] Chen X H, Liu Q, Luo K H and Wu L A 2009 *Opt. Lett.* **34** 695
[9] Liu X F, Chen X H, Yao X R, Yu W K, Zhai G J and Wu L A 2014 *Opt. Lett.* **39** 2314
[10] Radwell N, Mitchell K J, Gibson G M, Edgar M P, Bowman R and Padgett M J 2014 *Optica* **1** 285
[11] Zhang A X, He Y H, Wu L A, Chen L M and Wang B B 2018 *Optica* **5** 374
[12] He Y H, Zhang A X, Yu W K, Chen L M and Wu L A 2020 *Chin. Phys. Lett.* **37** 044208
[13] He Y H, Zhang A X, Li M F, Huang Y Y, Quan B G, Li D Z, Wu L A and Chen L M 2020 *APL Photon.* **5** 056102
[14] Jeltes T, McNamara J M, Hogervorst W, Vassen W, Krachmalnicoff V, Schellekens M, Perrin A, Chang H, Boiron D, Aspect A and Westbrook C I 2007 *Nature* **445** 402
[15] Li S, Cropp F, Kabra K, Lane T J, Wetzstein G, Musumeci P and Ratner D 2018 *Phys. Rev. Lett.* **121** 114801
[16] He Y H, Huang Y Y, Zeng Z R, Li Y F, Tan J H, Chen L M, Wu L A, Li M F, Quan B G, Wang S L and Liang T J 2021 *Sci. Bull.* **66** 133
[17] Chen X H, Agafonov I N, Luo K H, Liu Q, Xian R, Chekhova M V and Wu L A 2010 *Opt. Lett.* **35** 1166
[18] Ferri F, Magatti D, Lugiato L A and Gatti A 2010 *Phys. Rev. Lett.* **104** 253603
[19] Shapiro J H 2008 *Phys. Rev. A* **78** 061802
[20] Zhao C Q, Gong W L, Chen M L, Li, E R, Wang H, Xu D W and Han S S 2012 *Appl. Phys. Lett.* **101** 141123
[21] Katz O, Bromberg Y and Silberberg Y 2009 *Appl. Phys. Lett.* **95** 131110
[22] Shechtman Y, Gazit S, Szameit A, Eldar Y C and Segev M 2010 *Opt. Lett.* **35** 1148
[23] Luo K H, Huang B Q, Zheng W M and Wu L A 2012 *Chin. Phys. Lett.* **29** 074216
[24] Chen X H, Kong F H, Fu Q, Meng S Y and Wu L A 2017 *Opt. Lett.* **42** 5290
[25] Meng S Y, Sha Y H, Fu Q, Bao Q Q, Shi W W, Li G D, Chen X H and Wu L A 2018 *Opt. Lett.* **43** 4759
[26] Meng S Y, Shi W W, Tao J J, Fu Q, Bao Q Q, Sha Y H, Chen X H and Wu L A 2020 *Chin. Phys. B* **29** 128704

[27] Meng S Y, Chen M Y, Ji J, Shi W W, Fu Q, Bao Q Q, Chen X H and Wu L A 2022 *Chin. Phys. B* **31** 028702
[28] Lyu M, Wang W, Wang H, Wang H C, Li G W, Chen N and Situ G H 2017 *Sci. Rep.* **7** 17865
[29] He Y C, Wang G, Dong, G X, Zhu S T, Chen H, Zhang A X and Xu Z 2018 *Sci. Rep.* **8** 6469
[30] Horisaki R, Takagi R and Tanida J 2016 *Opt. Express* **24** 13738
[31] Yang H, Wu S, Wang H B, Cao D Z, Zhang S H, Xiong J and Wang K G 2018 *Phys. Rew. A* **98** 053853
[32] Cao D Z, Li Q C, Zhuang X C, Ren C, Zhang S H and Song X B 2018 *Chin. Phys. B* **27** 123401
[33] Leng J, Yu W K and Wang S F 2020 *Phys. Rew. A* **101** 033835
[34] Hu C Y, Zhu R G, Yu H and Han S S 2021 *Phys. Rew. A* **103** 043717
[35] Goodman J W 2020 *Speckle Phenomena in Optics: Theory and Applications*, 2nd edn. (Roberts & Company Publishers) pp. 68–78
[36] Goodman J W 2015 *Statistical Optics*, 2nd edn. (John Wiley & Sons, New York)
[37] Oh J E, Cho Y W, Scarcelli G and Kim Y H 2013 *Opt. Lett.* **38** 682
[38] Wang Y L, Wang F R, Liu R F, Chen D R, Gao H, Zhang P and Li F L 2015 *Opt. Lett.* **40** 5323
[39] Chen Z, Shi J, Li Y, Li Q and Zeng G 2014 *Eur. Phys. J. Appl. Phys.* **67** 10501
[40] Sun S, Liu W T, Gu J H, Lin H Z and Chen P X 2019 *Opt. Lett.* **44** 5993